Chemical Science

ROYAL SOCIETY OF CHEMISTRY

EDGE ARTICLE

View Article Online
View Journal | View Issue

Cite this: *Chem. Sci.*, 2026, **17**, 1624

All publication charges for this article have been paid for by the Royal Society of Chemistry

Insights into the initial steps of the thiamin pyrimidine synthase (ThiC)-catalyzed reaction through EPR spectroscopic characterization of radical intermediates

Melissa M. Bollmeyer, [a] Vishav Sharma, [b] Dmytro Fedoseyenko,[b] Yumeng Cao,[a] Guodong Rao, [a] Dean J. Tantillo, [a] Tadhg P. Begley *[b] and R. David Britt *[a]

Thiamin pyrimidine synthase (ThiC) is a noncanonical radical SAM enzyme that catalyzes the complex radical rearrangement of aminoimidazole ribonucleotide (AIR) to hydroxymethylpyrimidine phosphate (HMP-P) as part of the thiamin biosynthetic pathway in bacteria and plants. In this work, we investigate the mechanism of ThiC using advanced electron paramagnetic resonance (EPR) techniques. Freeze-quenching a reaction of ThiC revealed the accumulation of a new radical species. By employing electron nuclear double resonance (ENDOR) spectroscopy with various substrate isotopologues, we determined the hyperfine parameters of several nuclei, allowing us to propose a structure for this intermediate. The accumulated species was characterized as a dihydro-aminoimidazole centered radical attached to two ribose derived fragments. This radical is sensitive to perturbations in the enzyme H-bonding network. In addition, mutagenesis of active site residues results in the accumulation of two distinct intermediates, including a C5′ ribonucleotide centered radical and a ribose C2′ radical fragment. Identification of these early radical intermediates provides insights into the initial steps of the ThiC mechanism. The ThiC-catalyzed reaction involves a 20-step radical cascade and is the most complex rearrangement found in biosynthesis. This study highlights the pivotal role that EPR can play in elucidating the mechanism of highly complicated enzyme-catalyzed reactions.

Received 20th June 2025
Accepted 17th November 2025

DOI: 10.1039/d5sc04563k

rsc.li/chemical-science

Introduction

Thiamin pyrophosphate (TPP) is required by all organisms as a cofactor for enzymes involved in carbohydrate and amino acid catabolism.[1–5] In bacteria and plants, TPP is produced by separate biosynthetic routes to the pyrimidine and thiazole moieties.[6] The biosynthesis of the pyrimidine begins with the enzyme ThiC, a radical *S*-adenosylmethionine (SAM) enzyme that catalyzes the rearrangement of aminoimidazole ribonucleotide (AIR) to 4-amino-5-hydroxymethyl-2-methyl pyrimidine phosphate (HMP-P).[7] This remarkable reaction requires the most complicated radical cascade discovered in biosynthesis. *In vitro* reconstitution of this reaction has been achieved using recombinant ThiC, AIR, SAM, and a reductant.[7–11] By employing a set of ^{2}H and ^{13}C labeled AIR isotopologues, the repositioning of each atom in AIR to HMP-P has been determined (Fig. 1).[7,10] It was also shown that C1′ is lost as formate and C3′ is lost as carbon monoxide.

ThiC is a unique member of the radical SAM family, containing a CX_2CX_4C cluster binding motif rather than the canonical CX_3CX_2C motif.[9,11–13] Typically, radical SAM enzymes bind SAM at the unique iron of the cluster, cleaving it to yield L-methionine and a 5′-deoxyadenosyl radical (5′-dA$^{\bullet}$).[14,15] This radical is responsible for H-atom abstraction from the substrate to initiate further radical reactivity. Crystal structures of ThiC, however, show that the SAM analogue *S*-adenosylhomocysteine (SAH) or cleavage product L-Met bind to an additional transition metal site located 7 Å away from the cluster (Fig. S1A).[16] Interestingly, both 5′-H and 4′-H undergo H-atom abstraction, and deuterium labeling at these positions indicate that a single SAM molecule is used twice.[10] While other enzymes have been shown to use two equivalents of SAM,[17–19] ThiC is the only example where the same molecule of SAM is used for two H-atom abstractions from the same substrate molecule.

Recently, a detailed mechanistic study of ThiC based on the trapping of five intermediates led to the mechanism proposed in Fig. 1.[8] An early intermediate, **3**, is trapped as a shunt product when using an AIR analogue (**14**, Table S1) where the ribose is attached to imidazole at C4. A *Caulobacter crescentus* ThiC (*Cc*ThiC) E413Q mutation facilitated the characterization of intermediate **4**. The trapping of intermediate **5** using an *Arabidopsis thaliana* (*At*ThiC) D383A mutation suggests that cleavage of the C1′–C2′ bond occurs before the ribose fragment reattaches to the imidazole (**6**) to form intermediate **7**. Evidence for

[a]*Department of Chemistry, University of California–Davis, 1 Shields Ave., Davis, California 95616, USA. E-mail: rdbritt@ucdavis.edu*

[b]*Department of Chemistry, Texas A&M University, College Station, Texas 77842, USA. E-mail: begley@tamu.edu*

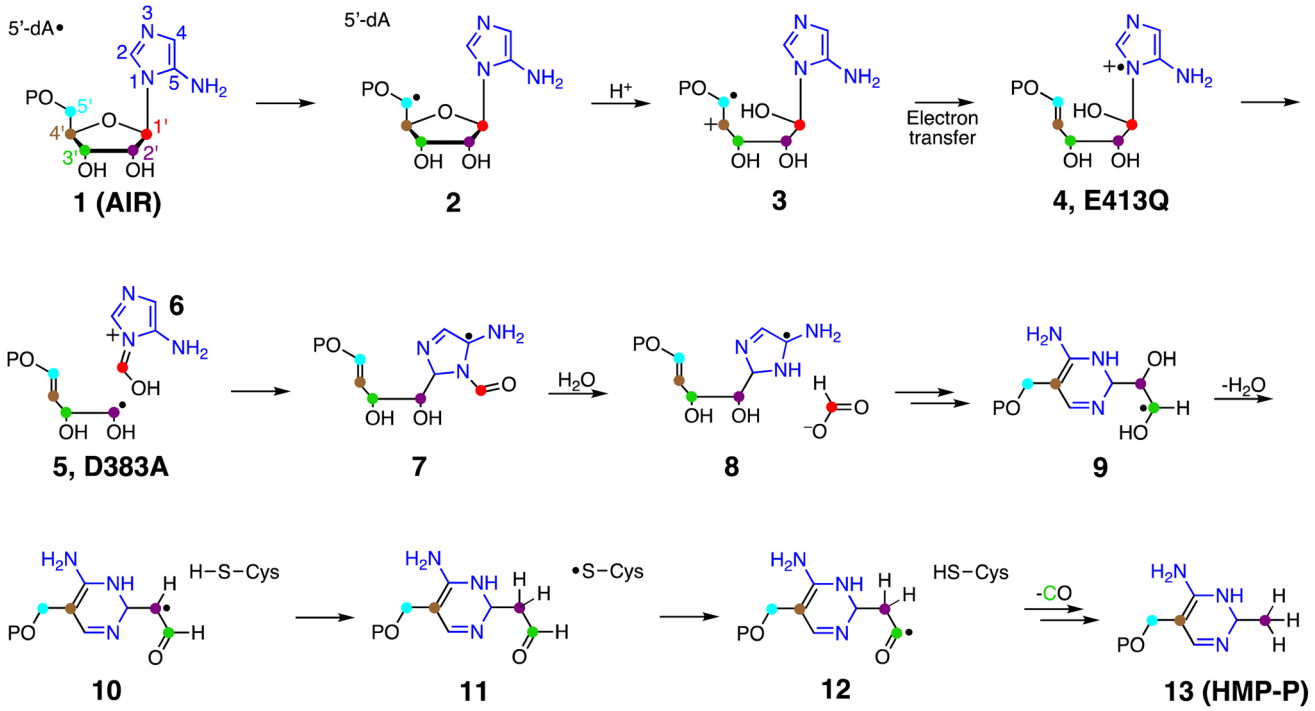

Fig. 1 The proposed mechanism of the ThiC-catalyzed rearrangement of AIR to HMP-P. For all the proposed steps, see ref. 8. Atoms derived from the aminoimidazole group are colored dark blue while those of the ribose are individually colored to help show their repositioning throughout the reaction. Intermediates **4** and **5** were trapped using the E413Q and D383A variants respectively.

the involvement of an active site *Cys* is provided by a *Cc*ThiC C474S mutant. This residue plays an essential role in radical-mediated H-atom transfer that initiates CO release. These results have laid the groundwork for understanding the complex 20-step ThiC mechanism, but many of the details remain uncertain.

To expand on our understanding of the ThiC mechanism, we aimed to trap and characterize radical intermediates using freeze-quenching and electron paramagnetic resonance (EPR) techniques. There have been a growing number of radical intermediates trapped and characterized during catalysis by radical SAM enzymes.[20–26] Of these, we recently identified an aminoimidazole radical intermediate of the enzyme BzaF.[27] A paralog of ThiC, BzaF catalyzes the radical rearrangement of AIR to 5-hydroxybenzimidazole (HBI) as part of the anaerobic cobalamin biosynthetic pathway.[28] Motivated by our success in characterizing an intermediate in the BzaF catalyzed reaction, we turned our attention to ThiC. Herein, we describe the characterization of a distinct intermediate formed by ThiC. Equipped with the ThiC mutants discussed above, we show the critical role of active-site electrostatic interactions on the ThiC mechanism.

Results and discussion

Accumulation of a substrate radical intermediate

Reducing ThiC with dithionite yields an $S = 3/2$ signal that could either be attributed to a high-spin cluster or to an $S = 1/2$ $[4Fe\text{-}4S]^{+}$ cluster antiferromagnetically coupled to an $S = 2$ Fe^{II} (Fig. S1B). While crystal structures show SAH binding to the extra Fe site, its role in catalysis remains unknown and is the subject of a future study. When reduced *At*ThiC is mixed with the substrates AIR and SAM, the $S = 3/2$ signal disappears concomitant with the formation of a new organic radical signal. Disappearance of the $S = 3/2$ signal suggests that the cluster becomes oxidized during catalysis. The radical signal is centered near $g = 2.004$ and accumulates over 6 minutes with an observed rate of 0.6 ± 0.1 min^{-1}, after which it begins to decay (Fig. S2A). While some fine structure is evident, there are likely many nuclei contributing hyperfine interactions (HFI) resulting in poorly resolved hyperfine features. The pulse Q-band echo-detected spectrum is consistent with a nearly isotropic signal centered at $g = 2.004$ (Fig. S2B).

In the absence of substrate AIR, a different radical species forms with better resolved hyperfine structure (Fig. S3). This radical signal has been observed previously and was attributed to a peptide backbone radical, likely on an α-carbon.[29] The backbone radical signal is not observed in the full reaction mixture when AIR is allowed to incubate before SAM is added. If instead SAM is added first for one minute followed by the addition of AIR, a mixture of the two radical species is obtained (Fig. S3). While the amino acid residue involved in backbone radical formation has not been identified, this residue is likely susceptible to off-pathway H-atom abstraction by 5′-dA• when AIR is not bound in the active site. When AIR is allowed to bind in the active site first, 5′-dA• reacts directly with AIR to initiate the radical rearrangement.[29]

To obtain more information on the HFI, we repeated the ThiC reaction using several ^{2}H AIR isotopologues (Table S1). Initial characterization by CW X-band EPR shows the most significant effects are from samples made in ^2H_2O or with 2,4-$^2H_2$ AIR (Fig. 2). When a proton contributing to the hyperfine structure is substituted by a deuteron, the hyperfine collapses by the proportion of their gyromagnetic ratios ($\gamma(^1H)/\gamma(^2H) = 6.5$). The collapse of the large hyperfine contributions when using the 2,4-$^2H_2$ AIR isotopologue is consistent with strong interactions (*ca.* 40 MHz and 60 MHz, see ENDOR section below) between the imidazole protons and the radical center, suggesting that the radical is located on or near the imidazole moiety. In addition, the major differences when ^2H_2O was used can be attributed to large exchangeable proton couplings (*ca.* 13 MHz and 25 MHz, see ENDOR). If the radical is centered on the imidazole moiety, the amine protons or an imidazole NH could be responsible for the observed couplings. Alternatively, the exchangeable proton couplings could arise from the ribose hydroxyl groups. We could also probe the proximity of the ribose to the radical center using AIR isotopologues selectively labeled with ^{13}C on the ribose. If a carbon carrying significant spin density is labeled with ^{13}C, the additional hyperfine interaction leads to broadening of the CW EPR spectrum. Using a 1′,2′,3′,4′,5′-^{13}C AIR isotopologue results in broadening by about 25 MHz (Fig. S4), suggesting that the ribose is attached to the radical center.

We propose that the accumulated intermediate would most likely be a radical centered on the electron-rich aminoimidazole moiety, which would be stabilized by resonance delocalization. A similar result was observed previously for BzaF, where a radical intermediate analogous to **4** was trapped and characterized by EPR techniques.[27] ThiC and BzaF are proposed to follow the same initial steps of AIR rearrangement, diverging after intermediate **5** where ThiC and BzaF catalyze C2′–C2 and C2′–C5 bond formation respectively.[8,30] It is possible that the accumulated ThiC radical is the same as that of BzaF. Two other aminoimidazole-centered radicals, intermediates **7** and **8**, are proposed to form during ThiC catalysis. These intermediates would have a similar stability to **4** and may therefore accumulate instead. To elucidate the structure of the trapped radical, we next sought to obtain quantitative HFI using a combination of selective isotope labeling and electron-nuclear double resonance (ENDOR) spectroscopy.

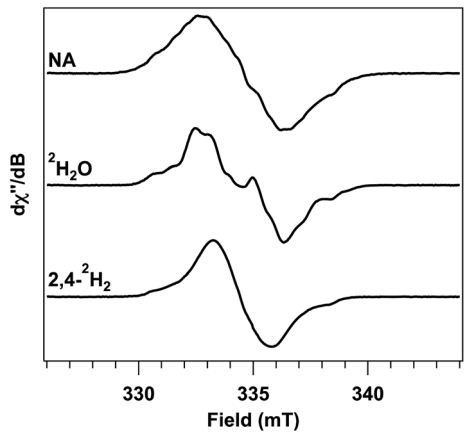

Fig. 2 CW X-band (9.4 GHz) EPR spectra obtained for reactions of *At*ThiC with AIR and dithionite initiated by addition of SAM and frozen after 6 minutes. Natural abundance (NA) AIR in H_2O and ^2H_2O, as well as a 2,4-$^2H_2$ AIR isotopologue were used. Conditions: temperature = 10 K, power = 0.2 mW, modulation amplitude = 2 G.

^{1}H and ^{2}H ENDOR of the radical intermediate

The CW EPR experiments discussed above clearly indicate the presence of multiple protons coupled to the radical. The Q-band ^{1}H Davies ENDOR spectrum for the natural abundance (NA) substrate radical collected at $g = 2.004$ contains at least four hyperfine-split doublets labeled a–d (Fig. 3A). When 2,4-$^2H_2$ AIR is used, the two doublets with the largest hyperfine couplings (c and d) disappear. A corresponding ^{2}H Davies ENDOR spectrum contains two signals that, when scaled to the frequency of ^{1}H, match doublets c and d. Thus, these two signals can be attributed to the imidazole 2-H and 4-H. Spectral simulations of the ^{2}H signals yield one dipolar hyperfine tensor with $A^2H = [3.7, 6.3, 7.4]$ MHz corresponding to signal c and one more isotropic tensor with $A^2H = [8.4, 9.0, 9.6]$ MHz corresponding to signal d. Quadrupolar splitting arising from the $I = 1$ spin of the deuteron is not resolved. Converting these tensors to the ^{1}H frequency gives $A^1H = [24.1, 41.0, 48.1]$ MHz and $A^1H = [54.7, 58.6, 62.4]$ MHz, respectively. The ^{1}H ENDOR spectrum is well simulated using these values (Fig. S5). The ^{2}H ENDOR spectrum more clearly shows the rhombicity of signal c, which overlaps with doublet b in the ^{1}H ENDOR spectrum. Such significant anisotropy is characteristic of through-space electron-nuclear dipole interactions experienced by protons attached to a spin-bearing sp^2 hybridized carbon (α-protons). Out-of-plane protons on a nucleus adjacent to the radical center (β-protons) tend to have more isotropic and conformation (dihedral angle)-dependent hyperfine tensors through the spin hyperconjugation mechanism.[31,32] Signal d is therefore consistent with a β-proton.

These hyperfine parameters are reminiscent of other characterized imidazole-centered radicals, including the BzaF radical intermediate, but a key distinction lies in the assignment of doublet d to a β-proton.[27,33,34] For the previously characterized imidazole-centered radicals, both 2-H and 4-H are in-plane with the π-system. Delocalization of the spin density onto their corresponding C-centers gives both of these protons significant anisotropy. Attachment of the ribose fragment to imidazole C2 for radicals **7** and **8** interrupts the π-system, where C2 is now an sp^3 center and 2-H is out-of-plane of the imidazole ring. As a result, 2-H would have considerably less anisotropy consistent with a β-proton. On this basis, we can narrow down the accumulated radical to either **7** or **8**, with doublet c assigned to 4-H and doublet d assigned to 2-H.

Having established the identity of doublets c and d, we next sought to characterize the HFI arising from solvent-exchangeable protons. When the reaction is prepared in ^2H_2O buffer, doublet a diminishes (Fig. 3B) and a corresponding ^{2}H doublet is observed in the ^{2}H Mims ENDOR spectrum. The Mims spectrum is best simulated using two ^{2}H HFI with $A^2H =$

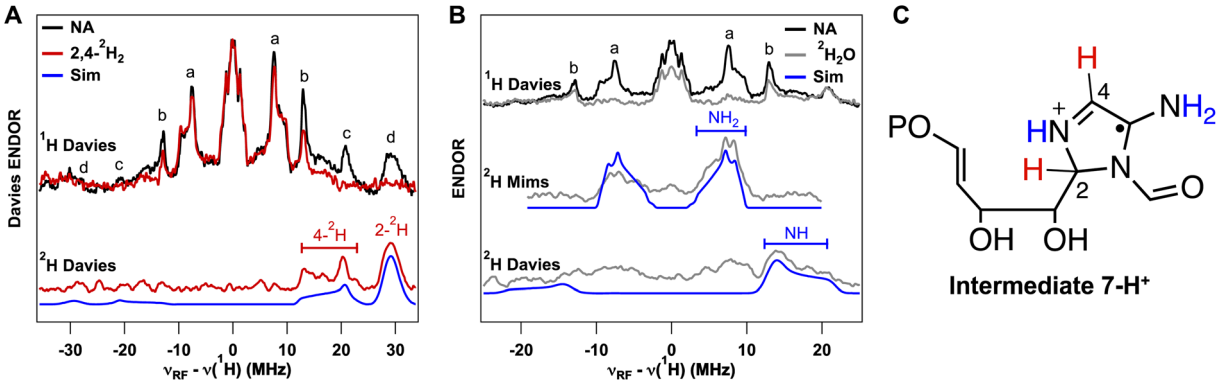

Fig. 3 (A) ^{1}H and ^{2}H Davies ENDOR spectra for the *At*ThiC reaction quenched after 6 minutes using NA AIR or 2,4-$^{2}H_2$ AIR. The ^{2}H Davies ENDOR spectrum for the 2,4-$^{2}H_2$ AIR sample was scaled to the frequency of ^{1}H for easier comparison. (B) ^{1}H Davies and frequency-scaled ^{2}H Davies and Mims ENDOR spectra comparing the NA AIR samples made in H_2O or $^{2}H_2O$. Experimental data are shown in black or grey. Spectral simulations are shown in blue. (C) The structure of proposed intermediate **7-H$^+$** with positions contributing to the observed HFI labeled in red and blue. Conditions: frequency = 34 GHz, temperature = 15 K. ^{1}H and ^{2}H Davies: $\pi/2$ = 12 ns, inversion pulse = 80 ns, τ = 300 ns. ^{2}H Mims: τ = 260 ns. Simulations: (A) A(2-^{2}H) = [8.4, 9.0, 9.6] MHz, A(4-^{2}H) = [3.7, 6.3, 7.4] MHz. (B) Mims: $A_1{}^{2}$H = [2.6, 0.7, 3.2] MHz, $A_2{}^{2}$H = [2.2, 3.1, 1.0] MHz. Davies: A^{2}H = [4.4, 6.8, 3.8] MHz.

[2.6, 0.7, 3.2] MHz and A^{2}H = [2.2, 3.1, 1.0] MHz. The lineshape of the ^{1}H Davies ENDOR signal for doublet a is slightly different from that of the ^{2}H Mims signal, partially owing to the suppression effect of Davies ENDOR close to 0 MHz. A simulation of the ^{1}H ENDOR spectrum yields a hyperfine tensor that is close to the scaled ^{2}H hyperfine tensor with A^{1}H = [15.7, 5.0, 21.0] and A^{1}H = [14.6, 19.9, 6.3] (Fig. S5). Given the large and nearly equal magnitude of a_{iso} (Table 1), they can be reasonably assigned to the two amine protons.

Another signal is observed in the ^{2}H Davies ENDOR spectrum that is not well resolved in the Mims spectrum. While Mims ENDOR is better suited for detecting small HFI, it is not as sensitive to large anisotropic HFI and is subject to blind spots called Mims holes. For this particular deuteron, Davies ENDOR provides a better method for measuring the larger hyperfine tensor due to the lack of Mims holes. The ^{2}H Davies ENDOR signal is simulated with A^{2}H = [4.4, 6.8, 3.8] MHz. Deuterium exchange for this proton is also evident in the difference ^{1}H ENDOR spectrum when the signals are scaled to doublet d (Fig. S5). Note that the central feature also loses intensity, which arises from more distant protons like solvent or amino acid side-chains. A simulation of the ^{1}H difference spectrum yields A^{1}H = [25.0, 25.0, 38.0] MHz. The most consistent position with such a large HFI would be a proton on a dihydroimidazole nitrogen. For intermediate **7**, the dihydroimidazole N3 could be protonated to give a cationic structure (denoted intermediate **7-H$^+$**, Fig. 3C). Alternatively, if the formyl group is lost to give intermediate **8**, the dihydroimidazole N1 could be protonated.

Other deuterium isotopologues, including 2′-^{2}H, 4′-^{2}H, and 5′,5′-$^{2}H_2$, do not yield any evident changes to the ^{1}H Davies ENDOR spectrum (Fig. S6). A sample made with 3′-^{2}H reveals a small HFI with A^{1}H = [2.8, 3.2, 5.4] (Fig. S7). The intensity of doublet b appears to be a combination of the 4-H anisotropic signal and the exchangeable proton assigned to an imidazole NH. The only unaccounted for proton is 1′-H, for which we did not have a deuterium isotopologue. Considering that the four largest hyperfine doublets are assigned, the 1′-H contribution is likely small.

Combining the ^{1}H and ^{2}H ENDOR data, we have obtained the hyperfine tensors of six protons summarized in Table 1. All values are reported as the absolute magnitude. Using these hyperfine values and an isotropic g-value of 2.004 produces a reasonable simulation of the X-band spectrum (Fig. S2C). These data are most consistent with a protonated imidazole-centered radical such as intermediate **7-H$^+$** or **8**.

Table 1 Experimental ^{1}H and ^{2}H HFI for reactions using WT *At*ThiC[a]

	$A(^{2}H)$ (MHz)		$A(^{1}H)$ (MHz)	
Position	[A_1, A_2, A_3]	a_{iso}	[A_1, A_2, A_3]	a_{iso}
2-H	8.4, 9.0, 9.6	9.0	54.7, 58.6, 62.4	58.6
4-H	3.7, 6.3, 7.4	5.8	24.1, 41.0, 48.1	37.7
NH_2	2.6, 0.7, 3.2	2.2	15.7, 5.0, 21.0	13.9
	2.2, 3.1, 1.0	2.1	14.6, 19.9, 6.3	13.6
N3-H	4.4, 6.8, 3.8	5.0	25.0, 25.0, 38.0	29.3
3′-H	—	—	2.8, 3.2, 5.4	3.8

[a] Errors are estimated to be ±0.1 MHz. For NH_2 the error of a_{iso} is estimated to be ±0.4 MHz and for NH the error is estimated to be ±3 MHz. The signs of experimental A tensors were not determined and are reported as the positive values.

^{13}C ENDOR of the radical intermediate

While a picture of an aminoimidazole centered radical is emerging, we next wanted to obtain quantitative HFI of the ribose carbon atoms to probe the attachment to imidazole. When the radical is generated using 1′,2′,3′,4′,5′-^{13}C labeled AIR, the ^{13}C ENDOR spectra contain features corresponding to one strongly coupled carbon and two weakly coupled carbons (Fig. 4). The strongly coupled signal is attributed to C2′ with A^{13}C = [21.8, 20.1, 20.0] MHz. Only the ν_+ branch of the ENDOR signal is observed because the intensity of the ν_- branch is

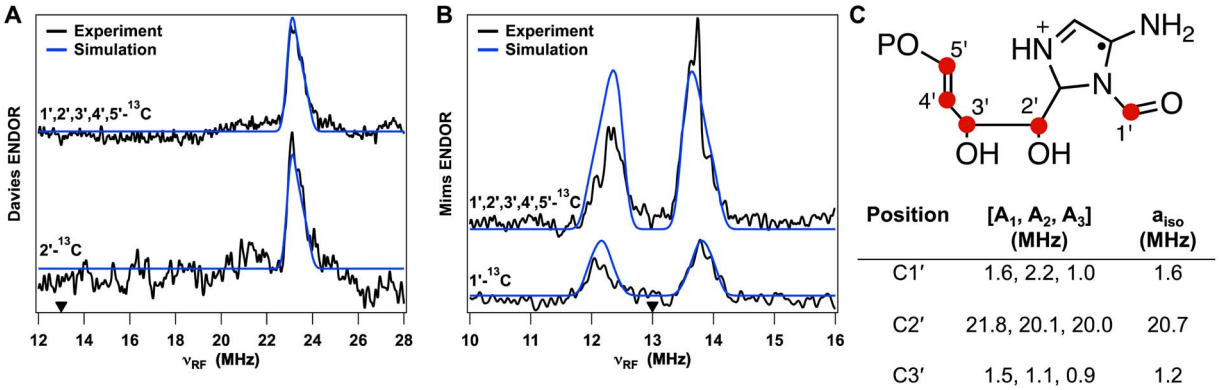

Position	$[A_1, A_2, A_3]$ (MHz)	a_{iso} (MHz)
C1′	1.6, 2.2, 1.0	1.6
C2′	21.8, 20.1, 20.0	20.7
C3′	1.5, 1.1, 0.9	1.2

Fig. 4 (A) ^{13}C Davies ENDOR spectra for the ThiC reaction using 1′,2′,3′,4′,5′-^{13}C and 2′-^{13}C labeled AIR. (B) ^{13}C Mims ENDOR spectra for the ThiC reaction using 1′,2′,3′,4′,5′-^{13}C and 1′-^{13}C labeled AIR. (C) HFI obtained from spectral simulations with their positions shown for the proposed intermediate **7-H$^+$**. Simulations are shown in blue. The ^{13}C Larmor frequency (13 MHz) is marked by a triangle. Conditions: frequency = 34 GHz, temperature = 15 K. ^{13}C Davies: $\pi/2 = 12$ ns, inversion pulse = 80 ns, $\tau = 300$ ns. ^{13}C Mims: $\tau = 260$ ns. Simulations: (A) $A^{13}C = [21.8, 20.1, 20.0]$ MHz. (B) Top: $A^{13}C = [1.6, 2.2, 1.0]$ MHz, [1.5, 1.1, 0.9] MHz. Bottom: $A^{13}C = [1.6, 2.2, 1.0]$ MHz.

suppressed by the low RF response close to 0 MHz. Nonetheless, this signal is sufficient to obtain the hyperfine tensor. The magnitude of the HFI suggests that this carbon is attached to the radical center, consistent with either intermediate **7** or **8**. One of the weakly coupled signals arises from C1′ with $A^{13}C = [1.6, 2.2, 1.0]$ MHz. The presence of an appreciable isotropic HFI from C1′ indicates a chemical bond to the radical species, thus narrowing down the possible intermediate to before the deformylation step. The remaining hyperfine doublet with $A^{13}C = [1.5, 1.1, 0.9]$ cannot be definitively assigned, but it is consistent with a carbon that is attached to a minor spin-carrying center like C2′. As such, we assign this doublet to C3′. The ^{13}C ENDOR data, taken together with the ^{1}H and ^{2}H ENDOR data, are best explained by intermediate **7-H$^+$**.

DFT calculated hyperfine parameters

To gain a better understanding of the structural features that could give rise to the observed hyperfine parameters, we used DFT to calculate the HFI of several possible structures (Table 2). While we assigned the structure to intermediate **7-H$^+$** based on the experimental HFI discussed above, we considered intermediates **4** and **7** in our calculations as well. For these calculations, we used a neutral phosphate group to avoid intramolecular interactions with the positively charged imidazole group. This provides a similar effect to the interactions observed in the crystal structure, where the phosphate group is held in place by H-bonding with active-site residues.[16] Some of the biggest differences arise at 2-H and 4-H. For the radical cation **4**, both 2-H and 4-H are predicted to have large and anisotropic HFI that can be attributed to significant spin density on both C2 (0.274) and C4 (0.295) and the planar orientation of both protons (Fig. 5). Intermediate **7**, which is a neutral dihydro-aminoimidazole radical, is predicted to have large isotropic hyperfine coupling from 2-H, but a small contribution from 4-H owing to minimal spin density at C4 (0.067). Thus, both intermediates **4** and **7** fail to explain the observed HFI of 2-H and 4-H. These HFI are better explained by **7-H$^+$**. This species is predicted to have greater spin delocalization onto C4 (0.251) similar to **4**, and small spin density on C2. In this case, the dihedral angle of 2-H allows for hyperconjugation with the radical center, which is delocalized over the N3–C4–C5 bonds. The significant spin density on N3 (0.251)

Table 2 Comparison of the experimental and DFT-predicted HFI for structures **4**, **7**, and **7-H+**[a]

	Experimental		Intermediate **4**		Intermediate **7**		Intermediate **7-H+**	
A (MHz)	$[A_1, A_2, A_3]$	$\lvert a_{iso}\rvert$	$[A_1, A_2, A_3]$	$\lvert a_{iso}\rvert$	$[A_1, A_2, A_3]$	$\lvert a_{iso}\rvert$	$[A_1, A_2, A_3]$	$\lvert a_{iso}\rvert$
2-^{1}H	54.7, 58.6, 62.4	58.6	−32.0, −45.5, −11.7	29.7	44.1, 46.5, 52.6	47.7	34.8, 43.6, 36.5	38.3
4-^{1}H	24.1, 41.0, 48.1	37.7	−31.3, −13.0, −46.3	30.2	−7.4, −5.2, 1.5	3.7	−25.9, −36.6, −7.8	23.4
N-^{1}H$_2$	15.7, 5.0, 21.0	13.9	−26.3, −38.0, −1.4	21.9	−7.6, −10.9, 6.0	4.2	−15.8, −0.2, −20.4	12.1
	14.6, 19.9, 6.3	13.6	−21.8, −35.1, 4.9	17.3	9.1, 4.4, 22.4	12.0	−12.2, −20.8, 3.5	9.8
N3-^{1}H	25.0, 25.0, 38.0	29.3	—	—	—	—	−26.9, −44.3, 1.3	23.3
3′-^{1}H	2.8, 3.2, 5.4	3.8	−0.3, −0.2, 0.9	0.1	1.2, −1.7, −0.1	0.2	−0.7, −1.4, 1.3	0.3
^{13}C1′	1.6, 2.2, 1.0	1.6	0.2, 0.8, 1.4	0.8	16.1, −2.9, −1.2	4.0	−2.0, −0.6, 4.7	0.7
^{13}C2′	21.8, 20.1, 20.0	20.6	−1.5, −1.1, −0.5	1.0	40.0, 31.4, 31.6	34.3	36.0, 26.5, 26.5	29.7

[a] Errors in experimental HFI are estimated to be ±0.1 MHz. For NH_2 the error of a_{iso} is estimated to be ±0.4 MHz and for NH the error is estimated to be ±3 MHz. The signs of experimental A tensors were not determined and are reported as the positive values. All a_{iso} values are reported as absolute magnitudes.

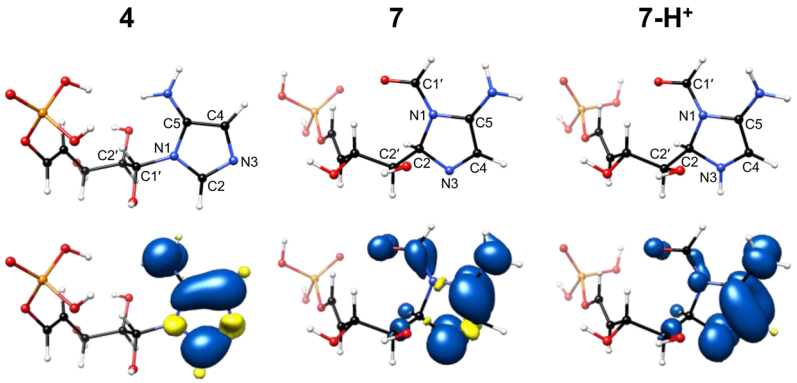

Atom	4	7	7-H$^+$
N1	-0.013	0.014	0.028
C2	0.274	0.019	0.017
N3	0.002	0.344	0.251
C4	0.295	0.067	0.251
C5	0.147	0.255	0.168
NH_2	0.234	0.110	0.135
C1′	-0.002	0.065	0.023
C2′	-0.001	0.018	0.019

Fig. 5 DFT predicted spin densities for intermediates **4**, **7**, and **7-H$^+$**. Spin density plots were generated using an isovalue of 0.003.

explains the large and isotropic hyperfine predicted for 2-H in this model. While the magnitude of a_{iso} is smaller than the observed value, variations in the dihedral angle and active site interactions could account for this difference.

Next, evaluating the exchangeable protons, the calculated HFI for the amine protons of **7** and **7-H$^+$** are close to the observed HFI, while those for **4** are calculated to be slightly greater. For **7-H$^+$**, the dihydroimidazole N3-H is predicted to have a large HFI with A^1H = [−26.9, −44.3, 1.3], which is similar in magnitude to the experimental A tensor but has larger anisotropy. The other proton HFI are all predicted to be less than 4 MHz. It is interesting to note that 3′-H was observed to have a_{iso} = 4 MHz, while DFT predicts a negligible a_{iso} of 0.3 MHz. This may be indicative of the ribose fragment being more conformationally constrained in the active site such that 3′-H is closer to the dihydroimidazole radical.

Another important distinction between intermediate **4** and **7-H$^+$** is the connection of the ribose fragment. For intermediate **4**, C2′ is farther from the radical and consequentially has a predicted a_{iso} < 1 MHz. In contrast, intermediate **7-H$^+$** has C2′ covalently attached to the dihydroimidazole C2. Therefore, the predicted HFI of C2′ for this structure is much closer to the experimental value with A^{13}C = [36.0, 26.5, 26.5] MHz. The neutral intermediate **7** is predicted to have a slightly larger magnitude HFI with A^{13}C = [40.0, 31.4, 31.6] MHz. While structural distortions in the active site could significantly impact the HFI of C2′, model **7-H$^+$** appears to be the most consistent with experimental values. The predicted C1′ hyperfine tensor is also close to the observed HFI with A^{13}C = [−2.0, −0.6, 4.7] MHz. Considering the DFT predicted ^{13}C and ^{1}H HFI, model **7-H$^+$** is in good agreement with the detected radical.

Mechanistic implications

Most of the reactions involved in the conversion of the AIR radical (**2**) to HMP-P (**13**) involve intrinsically fast radical fragmentation reactions that do not require enzymatic catalysis. It is therefore possible that the detection of the protonated form of intermediate **7** results from its accumulation due to a relatively slow deformylation step.

This reaction is likely to follow the expected well-characterized protease mechanism in which the amide carbonyl group is activated for nucleophilic attack by hydrogen bonding. However, since the conversion of AIR **1** to **7** involves a major rearrangement of the AIR atoms at the active site, it is not possible to reliably predict the active residues involved in the hydrolysis reaction. Another explanation could be that a slow protein conformational change, needed for the conversion of **7** to HMP-P (**13**), facilitates the detection of **7-H$^+$**.

The accumulation of intermediate **7-H$^+$** is an important distinction from the BzaF mechanism, where intermediate **4** is observed instead.[27] A homology model of BzaF based on the structure of *At*ThiC predicts that the active sites are highly conserved with only three differences affecting H-bonding to AIR.[28] Similarly, an AlphaFold2 predicted model of BzaF shows a very similar active site structure to ThiC (Fig. S8).[35,36] Despite having similar active sites, these enzymes are able to direct the high-energy intermediates to unique products. The accumulation of distinct radical intermediates provides one example of how the reactivity of these enzymes differ. Formation of **7-H$^+$** is the first step that diverges from the BzaF mechanism, where the C2′ radical adds to the imidazole C5 instead.[30] Determining how the active sites control radical addition to different positions of the imidazole fragment will provide insights into how these enzymes achieve their product selectivity.

DFT modeling of the mechanism

While the identification of **7-H$^+$** supports the proposed mechanism leading up to the loss of formate, we sought to investigate the energetic feasibility using DFT calculations at the M06-2X-D3/def2-SVP level of theory (see SI for details).[37–41] The AIR → **2** reaction (modeled using ethane as a hydrogen-atom donor) was predicted to have a free energy barrier of approximately 15 kcal mol^{-1}, while fragmentation of **4** to form **5** and **6** was predicted to be barrierless (from **4**). Recombination to form **7** could occur before or after deprotonation, but both scenarios were predicted to have low barriers: approximately 1 kcal mol^{-1} for the former and 8 kcal mol^{-1} for the latter. Consistent with previous studies,[8] the rate-determining step along the AIR → → → **7** pathway is predicted to be the initial hydrogen-atom transfer, and this step is predicted to have a low barrier. Thus, the pathway shown in Fig. 1 for formation of **7** appears to be feasible on energetic grounds. Following the formation of **7**, we

propose that a water molecule acts as a nucleophile attacking the amide to form a geminal diol. The uncatalyzed loss of formate from this intermediate was predicted to have a barrier of 20 kcal mol^{-1}, which would be feasible but likely slow. However, it is likely that this barrier could be greatly reduced by the enzyme active site. We therefore cannot yet deduce the factors contributing to the observed accumulation of **7-H$^+$**.

Identification of a C5′ radical using an E413Q mutant

With previous success in trapping several intermediates using ThiC mutants,[8] we hypothesized that we would be able to trap and characterize new radical intermediates using these same mutants. Freeze-quenching a reaction using an E413Q *Cc*ThiC mutant generates a new radical featuring a doublet centered around $g = 2.004$ with a large splitting of $a_{iso} = 74$ MHz (Fig. 6A). To characterize this new intermediate, we repeated measurements using 2,4-$^2H_2$, 3′-^{2}H, 4′-^{2}H, and 5′,5′-$^2H_2$ labeled AIR. Unlike the WT species, the 2,4-$^2H_2$ isotopologue does not affect the CW X-band spectrum, indicating that the radical is located on the ribose portion rather than the aminoimidazole. Minor contributions to the hyperfine structure are observed using the 3′-^{2}H and 4′-^{2}H isotopologues.

Initial reactions using 5′,5′-$^2H_2$ labeled AIR resulted in a new narrow feature centered within the doublet. Repeating this experiment with 3′,4′,5′,5′-$^2H_4$-labeled SAM results in complete collapse of the doublet signal. This suggests that a proton originating from the SAM molecule is contributing to the observed hyperfine splitting (*vide infra*). Further characterization of the radical generated with 5′,5′-$^2H_2$ AIR and NA SAM by ^{2}H Davies ENDOR reveals only one signal with $A^2H = [10.5, 11.3, 12.1]$ MHZ (Fig. 6B). This same signal is present when 3′,4′,5′,5′-$^2H_4$-labeled SAM is used, and no additional signals are observed. The corresponding ^{1}H HFI is not observed in the ^{1}H Davies ENDOR spectrum because it is larger than the range of frequencies allowed by the RF amplifier used in the experiment. A smaller ^{1}H HFI in the proton ENDOR can be assigned to 4′-H with $a_{iso} = 12.5$ MHz (Fig. 6C). We could not resolve the small HFI arising from 3′-H, but this could be due to low intensity of the ENDOR spectrum. The CW spectra could be reasonably simulated using the HFI obtained by ENDOR and $a_{iso} = 5$ MHz for 3′-H.

The large HFI of 5′-H and moderate HFI from 4′-H are consistent with a C5′ radical. Ribose radicals in DNA and RNA have been well characterized using radiation to generate radical species.[42–47] Typical EPR spectra of C5′ radicals feature one large

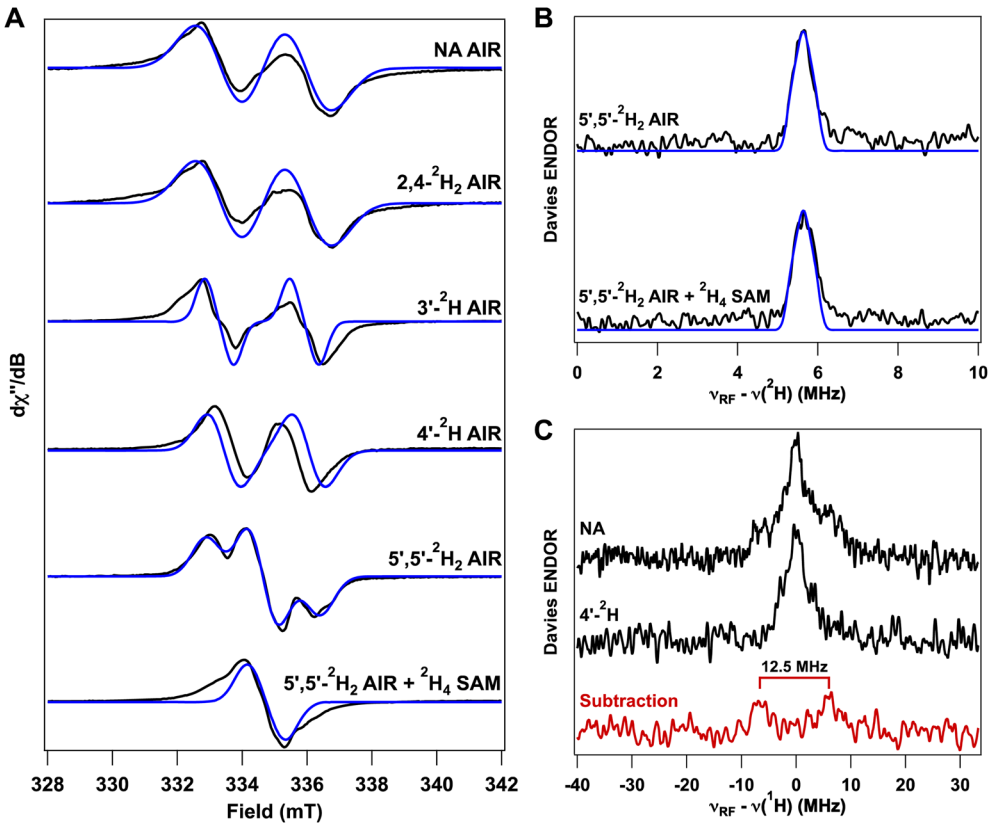

Fig. 6 EPR spectra for reactions using E413Q ThiC. Reactions used the same concentrations as the WT reactions and were frozen after 6 minutes. (A) CW X-band EPR spectra with AIR isotopologues. (B) ^{2}H Davies ENDOR spectra obtained at Q-band for reactions using 5′,5′-$^2H_2$ AIR. (C) ^{1}H Davies ENDOR spectra obtained at Q-band for reactions using either NA or 4′-^{2}H AIR. Experimental data is shown in black and spectral simulations are shown in blue. Conditions: (A) temperature = 10 K, power = 0.2 K, modulation amplitude = 2 G. (B and C) temperature = 15 K, $\pi/2$ = 12 ns, inversion pulse = 80 ns, $\tau = 300$ ns. Simulations were achieved using (A) A(5′-^{1}H) = [68.3,73.5,78.7], a_{iso}(4′-^{1}H) = 12.5 MHz, a_{iso}(3′-^{1}H) = 5 MHz or (B) A(5′-^{2}H) = [10.5, 11.3, 12.1] MHZ.

hyperfine contribution from 5′-H around 60 MHz.[46,48] The hyperfine contribution from 4′-H can vary depending on the conformation of the ring.[48,49] When 4′-H is in the nodal plane of the C5′ p-orbital, small hyperfine values are observed ranging from 6–17 MHz. If the ring becomes distorted such that 4′-H is no longer in this plane, much larger hyperfine values have been observed close to 100 MHz. This corresponds well to the relationship between the dihedral angle and the isotropic hyperfine of a β-proton. In our case, the small a_{iso} of 12.5 MHz is consistent with 4′-H being in the nodal position. To support our assignment of the E413Q radical species we also used the available ^{13}C AIR isotopologues. Significant broadening is observed using 1′,2′,3′,4′,5′-^{13}C AIR (Fig. S9), consistent with a radical centered on the AIR ribose. There is no broadening effect from 2′-^{13}C AIR, while minimal broadening is observed for 1′-^{13}C AIR. The larger ^{13}C couplings can then be attributed to the other C centers, likely C5′ and C4′, consistent with the assignment of a C5′ radical.

In the proposed ThiC mechanism, a C5′ radical (**2**) is formed by the initial H-atom abstraction. The accumulation of **2** could indicate that the Glu side-chain provides important electrostatic interactions with the aminoimidazole early in the mechanism, consistent with previous LC-MS results.[8] As shown in the crystal structure of *At*ThiC (Fig. 7), the Glu side-chain (E422, analogous to E413 in *Cc*ThiC) is only 3.3 Å from the aminoimidazole N1 of AIR.[16] Removal of the negative side-chain could result in destabilization of the radical cation **4**, leading to the accumulation of **2** rather than **7**-**H**$^+$. However, the assignment of the detected radical to **2** cannot explain the HFI originating from a proton on SAM. One possibility we considered was that **2** could undergo H/D exchange with 5′-dA. This scenario would not be feasible owing to the irreversibility of the H-atom abstraction and stereoselectivity for the 5′-proS position.[16] These results necessitate a different mechanism for H/D exchange, possibly involving an alternative C5′ radical (*e.g.* structure 72 in ref. 8). The origin of this unusual result is currently under investigation. Nonetheless, the detection of a C5′ radical when using the E413Q mutant shows that the electrostatic interactions provided by the Glu side-chain significantly influence the ThiC mechanism.

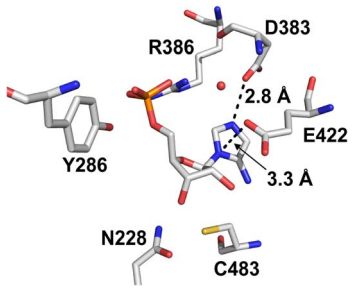

Fig. 7 Crystal structure of the *At*ThiC active site with AIR bound. Distances of E422 and D383 to the aminoimidazole group are labeled. PDB 4S27.[16]

Influence of H-bonding by D383

We next investigated the D383A *At*ThiC mutant, which previously allowed the trapping and characterization of intermediate **5** by LC-MS.[8] Repeating the ThiC reaction using the D383A mutant generates a radical signal unique from that of the WT reaction (Fig. 8A). Notably, there is a clear triplet splitting pattern consistent with two protons of similar hyperfine values *ca.* 30 MHz. While the CW signal appears to be a new radical species, the ^{1}H Davies ENDOR spectrum is similar to that of the WT *At*ThiC reaction (Fig. S10). Doublets a, b, and d are all still present with similar frequencies, while doublet c is more significantly influenced by the mutation. There is also an additional doublet with a_{iso} = 7.4 MHz labeled as doublet e. Using the 2,4-$^2H_2$ AIR isotopologue results in the disappearance of doublets c and d, analogous to the WT sample. Extracting the hyperfine tensor of doublet c yields A^1H = [34.4, 40.0, 44.2] MHz, corresponding to the dihydroimidazole 4-H as discussed for the WT sample. ENDOR spectra obtained using ^{13}C isotopologues are also similar to the corresponding WT *At*ThiC radical spectra (Fig. S10). The fully labeled ribose sample yields a single large hyperfine signal that is assigned to C2′.

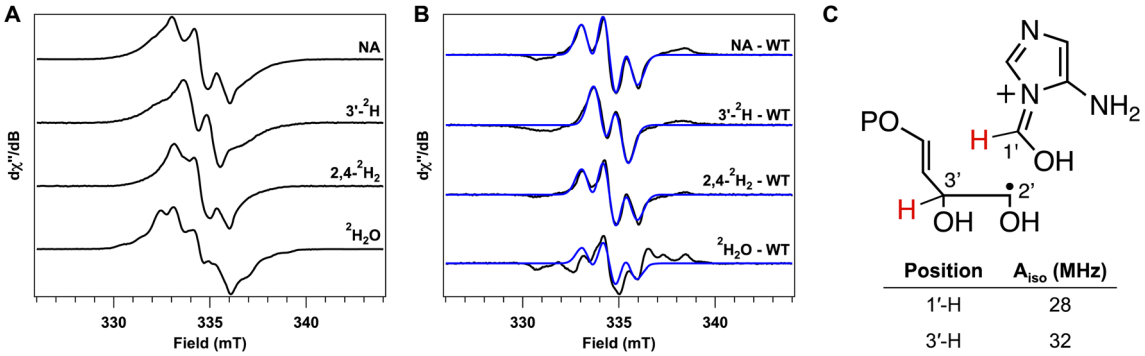

Fig. 8 Characterization of the intermediate trapped using D383A *At*ThiC. (A) CW X-band EPR spectra for the reaction using NA, 3′-^{2}H, 2,4-$^2H_2$ AIR and the reaction in ^2H_2O. (B) The same CW spectra after subtracting the corresponding WT spectra. Simulations are shown in blue. (C) Structure of radical **5** showing the assigned ^{1}H HFI. Conditions: temperature = 10 K, power = 0.2 mW, modulation amplitude = 2 G. Simulations were obtained using two isotropic proton HFI of 32 MHz and 28 MHz for the triplet spectra, and one proton HFI of 28 MHz for the doublet spectrum (3′-^{2}H).

Simulation of this spectrum gives a hyperfine tensor of $A^{13}C = [21.3, 22.1, 20.2]$. The isotropic component increased by 0.6 MHz compared to that of the WT *At*ThiC sample, indicating a minor increase in spin density at C2′. Like the WT radical, there are also two weakly coupled ^{13}C signals with $a_{iso} = ca.$ 1.2 MHz and 2.0 MHz.

The similarity in the ^{1}H and ^{13}C ENDOR spectra between D383A and WT *At*ThiC led us to reason that these features arise from the same intermediate **7-H$^+$**. These ENDOR features, however, do not explain the triplet splitting pattern observed in the CW spectrum. We could assign one of the protons contributing to the triplet as 3′-H, evidenced by the collapse of the triplet to a doublet when using the 3′-^{2}H isotopologue. The other proton could not be identified by any of the other available isotopologues and was not exchangeable. The only proton we could not test was 1′-H, so we can tentatively assign the other ~30 MHz splitting to this proton. These hyperfine signals are not apparent in the ^{1}H ENDOR spectrum, but if they arise from a second radical species, they may be buried under the signals attributed to **7-H$^+$**. Subtracting the CW spectrum of the WT reaction from that of D383A shows the triplet splitting pattern more clearly, which can be fit with two protons of $a_{iso} = 32$ MHz and 28 MHz (Fig. 8B). In these spectra, the ratio of the new radical to the WT radical was about 1.5 : 1. The spectrum using 3′-^{2}H fits well to a single proton of $a_{iso} = 28$ MHz. If we assign the 32 MHz signal to 3′-H and the 28 MHz signal to 1′-H, they can reasonably be β-protons to a C2′ centered radical. Intermediate **5** would be consistent with the proposed C2′ centered radical signal if C1′ is still in close proximity to C2′. Considering that the next step requires radical addition of C2′ to the imidazole C2, it is a good assumption that the radical of **5** remains close to the imidazole moiety. We therefore tentatively assign the triplet signal to radical **5**.

Differences in the HFI of the **7-H$^+$** radical compared to the WT sample, particularly the dihydroimidazole 4-H HFI, can be explained by a change in the conformation within the active site. The carboxylic group of D383 is only 2.8 Å away from the AIR imidazole N3 (Fig. 7). Removing the H-bonding interaction would reasonably affect the conformation of intermediates. Based on the accumulation of **5**, it was previously proposed that D383 is responsible for proton donation to the imidazole N3. Our results suggest that D383 is not the source of this proton because intermediate **7-H$^+$** can still accumulate. Consistent with the LC-MS studies, the observation of a mixture of **5** and **7-H$^+$** in the EPR spectrum suggests that the D383A mutation slows down the radical addition of **5** to the imidazole C2 of **6**. For this addition to occur, the aminoimidazole moiety would have to be repositioned in the active site. An alternative role of D383 may be to facilitate this repositioning through H-bonding. This Asp residue is one of the few differences between the ThiC and BzaF active sites, where it is replaced by an Asn in BzaF. The difference in H-bond interactions could aid in positioning the imidazole group for addition to either C2 in ThiC or C5 in BzaF.[28] Further investigations into the D383A mutant, along with other mutants, are currently underway. The influence of the D383A ThiC mutation on the accumulated radical species shows the significant role that H-bonding within the active site plays in facilitating the radical rearrangement of AIR.

Conclusions

We have detected and characterized a radical intermediate of the ThiC catalyzed rearrangement of AIR. EPR data reveal that this intermediate is the protonated form of structure **7**, suggesting that release of C1′ as formate is slow compared to the other radical addition/fragmentation steps. The structure of **7-H$^+$** is sensitive to disruptions in the H-bond network, exemplified by the effect of the D383A mutation on the HFI. While this residue is not responsible for proton donation to the imidazole N3, it may facilitate radical addition of intermediate **5** to **6** by positioning the aminoimidazole group. The aminoimidazole radical intermediate **4** has also been shown to be sensitive to the electrostatic interactions in the active site.[8] Using an E413Q *Cc*ThiC mutant, we trapped a C5′ radical that participates in unexpected H/D exchange with 5′-dA. This result demonstrates that the negatively charged side-chain of E413 plays a significant role during ThiC catalysis, likely by providing electrostatic stabilization of intermediates and positioning the substrate. As shown by these two mutants, interactions with active site residues play a critical role in guiding the ThiC mechanism. While the identification of these radicals has provided us a glimpse into the impressive control ThiC offers over the selective rearrangement of AIR, we are only beginning to understand all the factors involved in this complicated mechanism.

Experimental methods

Overexpression and purification

Arabidopsis thaliana ThiC, *Caulobacter crescentus* ThiC, and their variants were overexpressed and purified using the previously reported procedure.[8] The E413Q mutant of *Cc*ThiC was used instead of the corresponding mutant in *At*ThiC because of the low solubility of the *At*ThiC mutant. We note that *Cc*ThiC and *At*ThiC have similar structures and nearly identical active sites.[16,28] We therefore expect that the E413Q mutation in *Cc*ThiC is suitable to compare to the *At*ThiC reaction.[8]

Overexpression and purification of AIRs kinase

AIRs kinase from *Salmonella enterica* was overexpressed in *E. coli* B834(DE3) and purified using Ni-NTA chromatography per the published protocol.[50]

Synthesis of 5-aminoimidazole riboside (AIRs) and its isotopologues

AIRs and its isotopologues were synthesized according to the published procedures.[7,10,28] Enzymatic phosphorylation of AIRs (86) and its isotopologues was performed using the previously reported procedure.[8]

EPR sample preparation and spectral simulations

All samples were prepared in an anaerobic chamber (Coy Laboratories, 98% N_2, 2% H_2) with degassed buffers. For all

reactions, a total volume of 60 μL was used in 100 mM Tris pH 7.5 buffer. Final concentrations were 400 μM ThiC with 20 mM sodium dithionite, 1.5 mM AIR, and 3 mM SAM. A solution of the enzyme was first reduced with the dithionite and allowed to incubate for 10 minutes to ensure complete reduction. The enzyme was then incubated with the AIR substrate for 1 minute to allow for binding of the substrate. The reactions were initiated by the addition of SAM, transferred to a quartz tube (VitroCom; 2.4 mm outer diameter, 2.0 mm inner diameter), and frozen in liquid nitrogen after 6 minutes, unless otherwise noted. For samples prepared in ^2H_2O, the enzyme was buffer exchanged into a 100 mM Tris buffer in ^2H_2O (pD 7.5) by four rounds of washing with Amicon centrifugal filters. The reduced enzyme was allowed to incubate with AIR for 10 minutes to allow for deuterium exchange on the substrate. Spectral simulations were performed using EasySpin 6.0.4 in Matlab.[51]

Continuous wave EPR experiments

Continuous wave EPR measurements were carried out at X-band (~9.4 GHz) using a Bruker EleXsys E500 spectrometer equipped with a superhigh Q resonator (SHQE). Samples were kept at 10 K using an Oxford Instruments ESR900 continuous-flow liquid helium cryostat. Spectra were collected using a conversion time of 60 ms, modulation frequency of 100 kHz, modulation amplitude of 2 G, and microwave power of 0.2 mW. Number of scans was greater than 5 for all samples.

Pulse EPR experiments

All pulse EPR measurements were carried out at Q-band (34 GHz) using a Bruker ELEXSYS-E580 spectrometer equipped with a 10 W amplifier and an Oxford Instruments CF935 continuous-flow liquid helium cryostat. Samples were maintained at 15 K for all measurements. Field-swept spectra were obtained using the standard Hahn echo sequence (π/2–τ–π–τ–echo). ENDOR spectra were obtained using the standard Davies[52] pulse sequence for larger hyperfine couplings or the standard Mims[53] pulse sequence for smaller hyperfine couplings. For most measurements, the RF pulse amplification was applied using an ENI LPI10 (10–86 MHz) amplifier. For ^2H ENDOR measurements, an ENI A1000 (0.3–35 MHz) amplifier was used. All ENDOR spectra were collected at a field corresponding to $g = 2.004$. The number of scans was greater than 500 for all samples.

Density functional theory for hyperfine parameters

All DFT calculations were performed using ORCA version 5.0.4.[54] Geometry optimized structures were calculated using the BP86 functional. The def2-TZVPP basis set was used for all atoms with a def2/J and decontractaux auxiliary basis sets.[40,55] For EPR parameter calculations, the TPSSH functional was used in combination with the EPR-II and def2-TZVPP basis sets.[56,57] Becke–Johnson damping (D3BJ) was applied as a dispersion correction.[58,59] For all calculations, the RIJCOSX approximation[60] was applied and solvation was modeled using the conductor-like polarizable continuum model (CPCM)[61] with acetone. Initial models for geometry optimizations were built using Avogadro 1.2.0.[62] Spin density plots were generated using Chimera.[63]

Author contributions

RDB, TPB, MMB, and VS: conceptualization of the research project. MMB, VS, DF, and GR carried out experiments under the supervision of RDB and TPB. YC performed DFT calculations of the mechanism under supervision of DJT. MMB wrote the manuscript. All authors contributed to editing and revision of the manuscript.

Conflicts of interest

There are no conflicts of interest to declare.

Data availability

Coordinates for all computed structures are available at https://iochem-bd.bsc.es/browse/review-collection/100/438863/5b0dbba68a04a43dbb1d8c49.

The data supporting this article have been included as part of the supplementary information (SI). Supplementary information (SI): summary of mechanistic DFT calculations, substrate isotopologues, additional EPR spectra. See DOI: https://doi.org/10.1039/d5sc04563k.

Acknowledgements

RDB gratefully acknowledges funding support from NIH R35GM126961. TPB gratefully acknowledges funding support from the Robert A. Welch Foundation (A0034).

References

1 M. Rapala-Kozik, Vitamin B1 (Thiamine), *Adv. Bot. Res.*, 2011, **58**, 37–91, DOI: 10.1016/B978-0-12-386479-6.00004-4.
2 S. Manzetti, J. Zhang and D. Van Der Spoel, Thiamin Function, Metabolism, Uptake, and Transport, *Biochemistry*, 2014, **53**, 821–835, DOI: 10.1021/bi401618y.
3 F. Jordan, Current Mechanistic Understanding of Thiamin Diphosphate-Dependent Enzymatic Reactions, *Nat. Prod. Rep.*, 2003, **20**, 184–201, DOI: 10.1039/b111348h.
4 V. I. Bunik, A. Tylicki and N. V. Lukashev, Thiamin Diphosphate-Dependent Enzymes: From Enzymology to Metabolic Regulation, Drug Design and Disease Models, *FEBS J.*, 2013, **280**, 6412–6442, DOI: 10.1111/febs.12512.
5 S. Prajapati, F. Rabe Von Pappenheim and K. Tittmann, Frontiers in the Enzymology of Thiamin Diphosphate-Dependent Enzymes, *Curr. Opin. Struct. Biol.*, 2022, **76**, 102441, DOI: 10.1016/j.sbi.2022.102441.
6 C. T. Jurgenson, T. P. Begley and S. E. Ealick, The Structural and Biochemical Foundations of Thiamin Biosynthesis, *Annu. Rev. Biochem.*, 2009, **78**, 569–603, DOI: 10.1146/annurev.biochem.78.072407.102340.
7 B. G. Lawhorn, R. A. Mehl and T. P. Begley, Biosynthesis of the Thiamin Pyrimidine: The Reconstitution of

a Remarkable Rearrangement Reaction, *Org. Biomol. Chem.*, 2004, **2**, 2538, DOI: 10.1039/b405429f.

8 V. Sharma, D. Fedoseyenko, S. Joshi, S. Abdelwahed and T. P. Begley, Phosphomethylpyrimidine Synthase (ThiC): Trapping of Five Intermediates Provides Mechanistic Insights on a Complex Radical Cascade Reaction in Thiamin Biosynthesis, *ACS Cent. Sci.*, 2024, **10**, 988–1000, DOI: 10.1021/acscentsci.4c00125.

9 A. Chatterjee, Y. Li, Y. Zhang, T. L. Grove, M. Lee, C. Krebs, S. J. Booker, T. P. Begley and S. E. Ealick, Reconstitution of ThiC in Thiamine Pyrimidine Biosynthesis Expands the Radical SAM Superfamily, *Nat. Chem. Biol.*, 2008, **4**, 758–765, DOI: 10.1038/nchembio.121.

10 A. Chatterjee, A. B. Hazra, S. Abdelwahed, D. G. Hilmey and T. P. A. Begley, "Radical Dance" in Thiamin Biosynthesis: Mechanistic Analysis of the Bacterial Hydroxymethylpyrimidine Phosphate Synthase, *Angew. Chem., Int. Ed.*, 2010, **49**, 8653–8656, DOI: 10.1002/anie.201003419.

11 N. C. Martinez-Gomez and D. M. Downs, ThiC Is an [Fe-S] Cluster Protein That Requires AdoMet To Generate the 4-Amino-5-Hydroxymethyl-2-Methylpyrimidine Moiety in Thiamin Synthesis, *Biochemistry*, 2008, **47**, 9054–9056, DOI: 10.1021/bi8010253.

12 M. J. Dougherty and D. M. Downs, A Connection between Iron–Sulfur Cluster Metabolism and the Biosynthesis of 4-Amino-5-Hydroxymethyl-2-Methylpyrimidine Pyrophosphate in Salmonella Enterica, *Microbiol*, 2006, **152**, 2345–2353, DOI: 10.1099/mic.0.28926-0.

13 M. Raschke, L. Bürkle, N. Müller, A. Nunes-Nesi, A. R. Fernie, D. Arigoni, N. Amrhein and T. B. Fitzpatrick, Vitamin B1 Biosynthesis in Plants Requires the Essential Iron–Sulfur Cluster Protein, THIC, *Proc. Natl. Acad. Sci. U. S. A.*, 2007, **104**, 19637–19642, DOI: 10.1073/pnas.0709597104.

14 J. B. Broderick, B. R. Duffus, K. S. Duschene and E. M. Shepard, Radical *S* -Adenosylmethionine Enzymes, *Chem. Rev.*, 2014, **114**, 4229–4317, DOI: 10.1021/cr4004709.

15 B. M. Hoffman, W. E. Broderick and J. B. Broderick, Mechanism of Radical Initiation in the Radical SAM Enzyme Superfamily, *Annu. Rev. Biochem.*, 2023, **92**, 333–349, DOI: 10.1146/annurev-biochem-052621-090638.

16 M. K. Fenwick, A. P. Mehta, Y. Zhang, S. H. Abdelwahed, T. P. Begley and S. E. Ealick, Non-Canonical Active Site Architecture of the Radical SAM Thiamin Pyrimidine Synthase, *Nat. Commun.*, 2015, **6**, 6480, DOI: 10.1038/ncomms7480.

17 X. Ji, T. Mo, W. Liu, W. Ding, Z. Deng and Q. Zhang, Revisiting the Mechanism of the Anaerobic Coproporphyrinogen III Oxidase HemN, *Angew. Chem., Int. Ed.*, 2019, **58**, 6235–6238, DOI: 10.1002/anie.201814708.

18 R. M. Cicchillo, D. F. Iwig, A. D. Jones, N. M. Nesbitt, C. Baleanu-Gogonea, M. G. Souder, L. Tu and S. J. Booker, Lipoyl Synthase Requires Two Equivalents of *S* -Adenosyl- l -Methionine To Synthesize One Equivalent of Lipoic Acid, *Biochemistry*, 2004, **43**, 6378–6386, DOI: 10.1021/bi049528x.

19 T. L. Grove, J. S. Benner, M. I. Radle, J. H. Ahlum, B. J. Landgraf, C. Krebs and S. J. Booker, A Radically Different Mechanism for *S* -Adenosylmethionine–Dependent Methyltransferases, *Science*, 2011, **332**, 604–607, DOI: 10.1126/science.1200877.

20 T. A. Stich, W. K. Myers and R. D. Britt, Paramagnetic Intermediates Generated by Radical S-Adenosylmethionine (SAM) Enzymes, *Acc. Chem. Res.*, 2014, **47**, 2235–2243, DOI: 10.1021/ar400235n.

21 W. G. Walls, A. L. Vagstad, T. Delridge, J. Piel, W. E. Broderick and J. B. Broderick, Direct Detection of the α-Carbon Radical Intermediate Formed by OspD: Mechanistic Insights into Radical *S* -Adenosyl- l -Methionine Peptide Epimerization, *J. Am. Chem. Soc.*, 2024, **146**, 5550–5559, DOI: 10.1021/jacs.3c13829.

22 B. Ma, R. D. Britt and L. Tao, Radical SAM Enzyme PylB Generates a Lysyl Radical Intermediate in the Biosynthesis of Pyrrolysine by Using SAM as a Cofactor, *J. Am. Chem. Soc.*, 2024, **146**(10), 6544–6556, DOI: 10.1021/jacs.3c11266.

23 B. Ma, Y.-H. Lee, M. W. Ruszczycky, D. Ren, A. Engstrom, H. Liu and L. Tao, EPR Characterization of the BlsE Substrate Radical Offers Insight into the Determinants of Reaction Outcome That Distinguish Radical SAM Dioldehydratases from Dehydrogenases, *J. Am. Chem. Soc.*, 2025, **147**, 4111–4119, DOI: 10.1021/jacs.4c13307.

24 N. D. Lanz, J. M. Rectenwald, B. Wang, E. S. Kakar, T. N. Laremore, S. J. Booker and A. Silakov, Characterization of a Radical Intermediate in Lipoyl Cofactor Biosynthesis, *J. Am. Chem. Soc.*, 2015, **137**, 13216–13219, DOI: 10.1021/jacs.5b04387.

25 M. W. Ruszczycky, S. Choi, S. O. Mansoorabadi and H. Liu, Mechanistic Studies of the Radical *S* -Adenosyl- l -Methionine Enzyme DesII: EPR Characterization of a Radical Intermediate Generated During Its Catalyzed Dehydrogenation of TDP- d -Quinovose, *J. Am. Chem. Soc.*, 2011, **133**, 7292–7295, DOI: 10.1021/ja201212f.

26 J. M. Kuchenreuther, W. K. Myers, T. A. Stich, S. J. George, Y. NejatyJahromy, J. R. Swartz and R. D. Britt, A Radical Intermediate in Tyrosine Scission to the CO and CN^- Ligands of FeFe Hydrogenase, *Science*, 2013, **342**, 472–475, DOI: 10.1126/science.1241859.

27 D. M. Gagnon, T. A. Stich, A. P. Mehta, S. H. Abdelwahed, T. P. Begley and R. D. Britt, An Aminoimidazole Radical Intermediate in the Anaerobic Biosynthesis of the 5,6-Dimethylbenzimidazole Ligand to Vitamin B12, *J. Am. Chem. Soc.*, 2018, **140**, 12798–12807, DOI: 10.1021/jacs.8b05686.

28 A. P. Mehta, S. H. Abdelwahed, M. K. Fenwick, A. B. Hazra, M. E. Taga, Y. Zhang, S. E. Ealick and T. P. Begley, Anaerobic 5-Hydroxybenzimidazole Formation from Aminoimidazole Ribotide: An Unanticipated Intersection of Thiamin and Vitamin B_{12} Biosynthesis, *J. Am. Chem. Soc.*, 2015, **137**, 10444–10447, DOI: 10.1021/jacs.5b03576.

29 N. C. Martinez-Gomez, R. R. Poyner, S. O. Mansoorabadi, G. H. Reed and D. M. Downs, Reaction of AdoMet with ThiC Generates a Backbone Free Radical, *Biochemistry*, 2009, **48**, 217–219, DOI: 10.1021/bi802154j.

30 V. Sharma, S. Joshi, D. Fedoseyenko and T. P. Begley, 5-Hydroxybenzimidazole Synthase: Catalysis of a Complex

Radical Cascade in the Formation of the Axial Ligand B12, in review.
31 H. M. McConnell, C. Heller, T. Cole and R. W. Fessenden, Radiation Damage in Organic Crystals. I. $CH(COOH)_2$ in Malonic Acid[1], *J. Am. Chem. Soc.*, 1960, **82**, 766–775, DOI: 10.1021/ja01489a002.
32 R. W. Fessenden and R. H. Schuler, Electron Spin Resonance Studies of Transient Alkyl Radicals, *J. Chem. Phys.*, 1963, **39**, 2147–2195, DOI: 10.1063/1.1701415.
33 L. Kar and W. A. Bernhard, The Imidazole π Cation and Barbital π Anion Trapped in a Cocrystalline Complex X-Irradiated at 12 K: An ESR–ENDOR Study, *J. Chem. Phys.*, 1980, **73**, 3625–3631, DOI: 10.1063/1.440588.
34 F. Q. Ngo, E. E. Budzinski and H. C. Box, Free Radical Formation in X-Irradiated Histidine HCl, *J. Chem. Phys.*, 1974, **60**, 3373–3377, DOI: 10.1063/1.1681543.
35 J. Jumper, R. Evans, A. Pritzel, T. Green, M. Figurnov, O. Ronneberger, K. Tunyasuvunakool, R. Bates, A. Žídek, A. Potapenko, A. Bridgland, C. Meyer, S. A. A. Kohl, A. J. Ballard, A. Cowie, B. Romera-Paredes, S. Nikolov, R. Jain, J. Adler, T. Back, S. Petersen, D. Reiman, E. Clancy, M. Zielinski, M. Steinegger, M. Pacholska, T. Berghammer, S. Bodenstein, D. Silver, O. Vinyals, A. W. Senior, K. Kavukcuoglu, P. Kohli and D. Hassabis, Highly Accurate Protein Structure Prediction with AlphaFold, *Nature*, 2021, **596**, 583–589, DOI: 10.1038/s41586-021-03819-2.
36 M. Mirdita, K. Schütze, Y. Moriwaki, L. Heo, S. Ovchinnikov and M. Steinegger, ColabFold: Making Protein Folding Accessible to All, *Nat. Methods*, 2022, **19**, 679–682, DOI: 10.1038/s41592-022-01488-1.
37 Y. Zhao and D. G. Truhlar, The M06 Suite of Density Functionals for Main Group Thermochemistry, Thermochemical Kinetics, Noncovalent Interactions, Excited States, and Transition Elements: Two New Functionals and Systematic Testing of Four M06-Class Functionals and 12 Other Functionals, *Theor. Chem. Acc.*, 2008, **120**, 215–241, DOI: 10.1007/s00214-007-0310-x.
38 Y. Zhao and D. G. Truhlar, Density Functionals with Broad Applicability in Chemistry, *Acc. Chem. Res.*, 2008, **41**, 157–167, DOI: 10.1021/ar700111a.
39 N. Mardirossian and M. Head-Gordon, How Accurate Are the Minnesota Density Functionals for Noncovalent Interactions, Isomerization Energies, Thermochemistry, and Barrier Heights Involving Molecules Composed of Main-Group Elements?, *J. Chem. Theory Comput.*, 2016, **12**, 4303–4325, DOI: 10.1021/acs.jctc.6b00637.
40 F. Weigend, Accurate Coulomb-Fitting Basis Sets for H to Rn, *Phys. Chem. Chem. Phys.*, 2006, **8**, 1057, DOI: 10.1039/b515623h.
41 S. Grimme, A. Hansen, J. G. Brandenburg and C. Bannwarth, Dispersion-Corrected Mean-Field Electronic Structure Methods, *Chem. Rev.*, 2016, **116**, 5105–5154, DOI: 10.1021/acs.chemrev.5b00533.
42 A. Adhikary, D. Khanduri, A. Kumar and M. D. Sevilla, Photoexcitation of Adenine Cation Radical $[A^{\bullet+}]$ in the near UV-vis Region Produces Sugar Radicals in Adenosine and in Its Nucleotides, *J. Phys. Chem. B*, 2008, **112**, 15844–15855, DOI: 10.1021/jp808139e.
43 L. I. Shukla, R. Pazdro, J. Huang, C. DeVreugd, D. Becker and M. D. Sevilla, The Formation of DNA Sugar Radicals from Photoexcitation of Guanine Cation Radicals, *Radiat. Res.*, 2004, **161**, 582–590, DOI: 10.1667/RR3167.
44 A. Adhikary, UVA-Visible Photo-Excitation of Guanine Radical Cations Produces Sugar Radicals in DNA and Model Structures, *Nucleic Acids Res.*, 2005, **33**, 5553–5564, DOI: 10.1093/nar/gki857.
45 D. Khanduri, S. Collins, A. Kumar, A. Adhikary and M. D. Sevilla, Formation of Sugar Radicals in RNA Model Systems and Oligomers *via* Excitation of Guanine Cation Radical, *J. Phys. Chem. B*, 2008, **112**, 2168–2178, DOI: 10.1021/jp077429y.
46 A. Adhikary, C5'- and C3'-Sugar Radicals Produced *via* Photo-Excitation of One-Electron Oxidized Adenine in 2'-Deoxyadenosine and Its Derivatives, *Nucleic Acids Res.*, 2006, **34**, 1501–1511, DOI: 10.1093/nar/gkl026.
47 A. Adhikary, D. Becker and M. D. Sevilla, Electron Spin Resonance of Radicals in Irradiated DNA, in. *Applications of EPR in Radiation Research*, eds. Lund, A. and Shiotani, M., Springer International Publishing, Cham, 2014, pp. 299–352, DOI: 10.1007/978-3-319-09216-4_8.
48 A. Adhikary, D. Becker, B. J. Palmer, A. N. Heizer and M. D. Sevilla, Direct Formation of the C5′-Radical in the Sugar–Phosphate Backbone of DNA by High-Energy Radiation, *J. Phys. Chem. B*, 2012, **116**, 5900–5906, DOI: 10.1021/jp3023919.
49 E. O. Hole, W. H. Nelson, E. Sagstuen and D. M. Close, Free Radical Formation in Single Crystals of 2′-Deoxyguanosine 5′-Monophosphate Tetrahydrate Disodium Salt: An EPR/ENDOR Study, *Radiat. Res.*, 1992, **129**, 119, DOI: 10.2307/3578149.
50 Y. Zhang, M. Dougherty, D. M. Downs and S. E. Ealick, Crystal Structure of an Aminoimidazole Riboside Kinase from Salmonella Enterica, *Structure*, 2004, **12**, 1809–1821, DOI: 10.1016/j.str.2004.07.020.
51 S. Stoll and A. Schweiger, EasySpin, a Comprehensive Software Package for Spectral Simulation and Analysis in EPR, *J. Magn. Reson.*, 2006, **178**, 42–55, DOI: 10.1016/j.jmr.2005.08.013.
52 E. R. Davies, A New Pulse Endor Technique, *Phys. Lett. A*, 1974, **47**, 1–2, DOI: 10.1016/0375-9601(74)90078-4.
53 W. B. Mims, Pulsed Endor Experiments, *Proc. R. Soc. London, Ser. A*, 1965, **283**, 452–457, DOI: 10.1098/rspa.1965.0034.
54 F. Neese, The ORCA Program System, *Comput. Mol. Biosci.*, 2012, **2**(1), 73–78, DOI: 10.1002/wcms.81.
55 F. Weigend and R. Ahlrichs, Balanced Basis Sets of Split Valence, Triple Zeta Valence and Quadruple Zeta Valence Quality for H to Rn: Design and Assessment of Accuracy, *Phys. Chem. Chem. Phys.*, 2005, **7**, 3297, DOI: 10.1039/b508541a.
56 V. Barone, Structure, Epr Parameters, and Reactivity of Organic Free Radicals from a Density Functional Approach, *Theor. Chim. Acta*, 1995, **91**, 113–128, DOI: 10.1007/BF01114980.

57 N. Rega, M. Cossi and V. Barone, Development and Validation of Reliable Quantum Mechanical Approaches for the Study of Free Radicals in Solution, *J. Chem. Phys.*, 1996, **105**, 11060–11067, DOI: 10.1063/1.472906.

58 S. Grimme, J. Antony, S. Ehrlich and H. Krieg, A Consistent and Accurate *Ab Initio* Parametrization of Density Functional Dispersion Correction (DFT-D) for the 94 Elements H-Pu, *J. Chem. Phys.*, 2010, **132**, 154104, DOI: 10.1063/1.3382344.

59 S. Grimme, S. Ehrlich and L. Goerigk, Effect of the Damping Function in Dispersion Corrected Density Functional Theory, *J. Comput. Chem.*, 2011, **32**, 1456–1465, DOI: 10.1002/jcc.21759.

60 F. Neese, F. Wennmohs, A. Hansen and U. Becker, Efficient, Approximate and Parallel Hartree–Fock and Hybrid DFT Calculations. A 'Chain-of-Spheres' Algorithm for the Hartree–Fock Exchange, *Chem. Phys.*, 2009, **356**, 98–109, DOI: 10.1016/j.chemphys.2008.10.036.

61 A. Klamt and G. Schüürmann, COSMO: A New Approach to Dielectric Screening in Solvents with Explicit Expressions for the Screening Energy and Its Gradient, *J. Chem. Soc., Perkin Trans. 2*, 1993, **2**(5), 799–805, DOI: 10.1039/P29930000799.

62 M. D. Hanwell, D. E. Curtis, D. C. Lonie, T. Vandermeersch, E. Zurek and G. R. A. Hutchison, An Advanced Semantic Chemical Editor, Visualization, and Analysis Platform, *J. Cheminf.*, 2012, **4**, 17, DOI: 10.1186/1758-2946-4-17.

63 E. F. Pettersen, T. D. Goddard, C. C. Huang, G. S. Couch, D. M. Greenblatt, E. C. Meng and T. E. Ferrin, UCSF Chimera—A Visualization System for Exploratory Research and Analysis, *J. Comput. Chem.*, 2004, **25**, 1605–1612, DOI: 10.1002/jcc.20084.